

Time and space resolved interferometry for laser-generated fast electron measurements

P. Antici, S. N. Chen, L. Gremillet, T. Grismayer, P. Mora, P. Audebert, and J. Fuchs

Citation: [Review of Scientific Instruments](#) **81**, 113302 (2010); doi: 10.1063/1.3499250

View online: <http://dx.doi.org/10.1063/1.3499250>

View Table of Contents: <http://scitation.aip.org/content/aip/journal/rsi/81/11?ver=pdfcov>

Published by the [AIP Publishing](#)

Articles you may be interested in

[Combined x-ray scattering, radiography, and velocity interferometry/streaked optical pyrometry measurements of warm dense carbon using a novel technique of shock-and-releasea\)](#)

Phys. Plasmas **21**, 056309 (2014); 10.1063/1.4876613

[Dense electron-positron plasmas and bursts of gamma-rays from laser-generated quantum electrodynamic plasmasa\)](#)

Phys. Plasmas **20**, 056701 (2013); 10.1063/1.4801513

[Development of a Nomarski-type multi-frame interferometer as a time and space resolving diagnostics for the free electron density of laser-generated plasma](#)

Rev. Sci. Instrum. **83**, 043501 (2012); 10.1063/1.3701366

[Time and space resolved visible spectroscopic imaging CO2 laser produced extreme ultraviolet emitting tin plasmas](#)

J. Appl. Phys. **111**, 063304 (2012); 10.1063/1.3698628

[Effect of density profile on beam control of intense laser-generated fast electrons](#)

Phys. Plasmas **17**, 063103 (2010); 10.1063/1.3432695



OXFORD
INSTRUMENTS
The Business of Science®

**'On the way to a
graphene spin field effect transistor'**
by Prof. Barbaros and the Özyilmaz Group at National University of Singapore

Download a FREE application note

Time and space resolved interferometry for laser-generated fast electron measurements

P. Antici,^{1,2,a)} S. N. Chen,³ L. Gremillet,⁴ T. Grismayer,⁵ P. Mora,⁵ P. Audebert,² and J. Fuchs^{2,b)}

¹*Istituto Nazionale di Fisica Nucleare, Via E. Fermi, Frascati 40-00044, Italy; ILE-Ecole Polytechnique-CNRS-ENSTA-Iogs-UP Sud, Batterie de l'Yvette, Palaiseau 91761, France; and Dipartimento di Scienze di Base e Applicate per l'Ingegneria, Sapienza-Università di Roma, Via A. Scarpa 14, Roma 00161, Italy*

²*LULI, École Polytechnique, CNRS, CEA, UPMC, route de Saclay, Palaiseau 91128, France*

³*Livermore National Laboratory, L-209, P.O. Box 808, Livermore, California 94550, USA*

⁴*CEA, DAM, DIF, Arpajon, F-91297, France*

⁵*Centre de Physique Théorique, École Polytechnique, CNRS, Palaiseau 91128, France*

(Received 4 August 2010; accepted 16 September 2010; published online 30 November 2010)

A technique developed to measure in time and space the dynamics of the electron populations resulting from the irradiation of thin solids by ultraintense lasers is presented. It is a phase reflectometry technique that uses an optical probe beam reflecting off the target rear surface. The phase of the probe beam is sensitive to both laser-produced fast electrons of low-density streaming into vacuum and warm solid density electrons that are heated by the fast electrons. A time and space resolved interferometer allows to recover the phase of the probe beam sampling the target. The entire diagnostic is computationally modeled by calculating the probe beam phase when propagating through plasma density profiles originating from numerical calculations of plasma expansion. Matching the modeling to the experimental measurements allows retrieving the initial electron density and temperature of both populations locally at the target surface with very high temporal and spatial resolution (~ 4 ps, $6 \mu\text{m}$). Limitations and approximations of the diagnostic are discussed and analyzed. © 2010 American Institute of Physics. [doi:10.1063/1.3499250]

I. INTRODUCTION

Laser acceleration of particles using high intensity short pulse lasers is a field of growing interest for science and applications. For example, several schemes have been proposed to perform fast ignition of inertial confinement targets (ICF) (Ref. 1) using secondary particle sources generated from solids such as electrons² or protons.³ More generally, the variety of secondary sources (γ -rays, ions, x-rays) that can be generated by hot (MeV) electrons produced in the interaction between ultraintense lasers and solids offer new prospects to generate or probe a wide range of states of matter.

These electrons, with energies ~ 1 MeV, are generated at the critical density interface of the solid targets, and are common for on-target laser intensities of 10^{19} W/cm². Their mean free path (~ 1 mm) is much longer compared to the common target thickness (~ 10 s of μm). Having propagated through the target, they subsequently expand into vacuum,⁴ together with ions that they electrostatically accelerate from the target rear surface to MeV energies.⁵ Besides accelerating ions, the hot electrons also transfer part of their energy during their transport through the target, via collisional and collective processes, to the target bulk (initially

cold but then becoming warm) electron population and may thus be heated up to temperatures ranging from eV to keV.⁶ This allows generating so-called warm dense matter states,^{7–9} which are necessary for ICF or astrophysics studies. Analyzing the spatial and temporal properties of these hot electrons, including the characteristics of their propagation in dense targets, is therefore crucial for all above mentioned applications.

Here we describe a technique that allows us to measure, in time and space, at the target rear, the characteristics of both the hot (having density less than critical) and bulk (i.e., at solid density) electron populations resulting from the interaction between intense lasers and solids. It exploits time-resolved phase measurements of an optical probe beam reflecting off the solid rear surface.¹⁰ Indeed, as the probe propagates through the cloud of low-density hot electrons streaming into vacuum before being reflected back from the moving warm solid, its phase is changed according to the characteristics of both (hot and warm bulk) electron populations. This diagnostic, based on time and space resolved interferometry, and therefore in the following called TASRI, allows us to access directly and locally the initial electron density and temperature of the hot (low-density) electrons (n_h^0, T_h^0) as well as the initial temperature of warm (solid density) bulk electrons (T_c^0) at the moment when the hot electrons initiate plasma expansion, as well as the subsequent evolution of these parameters. Up to now, information about the electron generation and transport through solids had been

^{a)}Author to whom correspondence should be addressed. Electronic mail: patrizio.antici@polytechnique.edu.

^{b)}Electronic mail: julien.fuchs@polytechnique.fr.

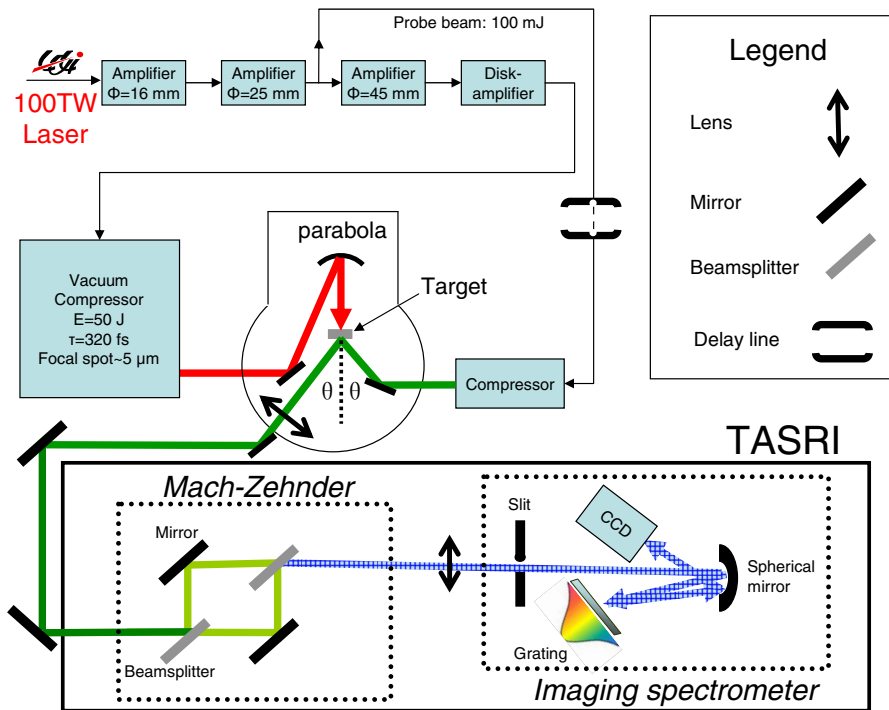


FIG. 1. (Color online) Experimental setup showing the main beam, the target, the probe beam reflecting off the target and the interferometer (in gray shaded box).

obtained indirectly through different methods, such as high-energy electron spectrometry,^{11–14} optical transition¹⁵ or Cherenkov¹⁶ radiation induced by highly energetic electrons, x-ray ($K\alpha$) emission,^{17,18,11,13,19,20} Bremsstrahlung emission,^{17,19} nuclear activation,²¹ reflectivity measurements,¹⁸ and self-emission.^{18,22}

Unfortunately, the aforementioned diagnostics (x-ray Bremsstrahlung, transition or Cherenkov radiation emission, nuclear activation, and $K\alpha$ emission) are time and/or space integrated. As a result, they cannot access the hot electron dynamics which can then only be investigated through simulations. This is a significant limitation compared to what the presented diagnostic can offer. The here presented diagnostic alleviates these limitations by allowing a local measurement of these hot electron dynamics, with a temporal resolution of ~ 4 ps and a spatial resolution of ~ 6 μm .

The paper is organized as follows. Section II details the diagnostic. Section II A presents technical information about the measurement setup and the interferometer. In Sec II B we discuss the way the probe beam phase is affected by the plasma expansion into vacuum. Section II C details the methodology used to infer the characteristics of both hot and warm (bulk) electron populations from the phase measurements (n_h^0, T_h^0, T_c^0). Finally, Sec. III presents some measurements and concludes the study.

II. DESCRIPTION OF THE DIAGNOSTIC AND OF THE METHODOLOGY

A. Setup of diagnostic

The TASRI diagnostic is based on the measurement of the phase of a probe beam (see Fig. 1) reflecting off the rear surface of a target irradiated by a main, high-intensity, laser beam. The measurements were performed on the 100 TW laser facility at LULI. The probe beam was a pick-off from the main beam at the same wavelength (in our case λ_p

$= 1.057$ μm) and with diameter about 16 mm, energy of about 100 mJ, chirped linearly to about 50 ps, and incident on target with $\theta = 45^\circ$. With a micrometric timeslide it was possible to change the delay between the main beam and the probe beam with a precision of < 1 ps. Since the target needs to reflect the incident probe beam, we used aluminum foils with thickness 25 μm and very high quality reflectivity, i.e., targets with mirrorlike optical surface allowing specular reflection with significant quality. As shown in Fig. 1, the image of the target surface, illuminated by the probe beam, was collected, after reflection from the target rear surface, by a lens and sent to the TASRI diagnostic.

The image of the target surface was made to coincide with the entrance plane of a Mach–Zehnder interferometer. The latter creates an interference pattern in the zone where the two beams in the output overlap (see Fig. 2). This image is further relayed on the entrance slit of the imaging spectrometer which will select a fraction of the imaged rear target surface, typically a few micrometers large. With the slit, we

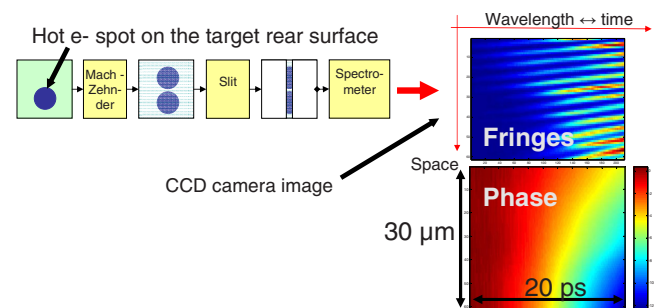


FIG. 2. (Color online) Working principle of the TASRI: the plasma expansion on the rear target surface (see Fig. 3) is imaged by the probe beam, goes through a Mach–Zehnder, and is selected by a slit. A central slice of the image is passed through a spectrometer to have time information exploiting the linear chirp of the probe beam. A motion of the fringes corresponds to a phase shift at the target rear surface.

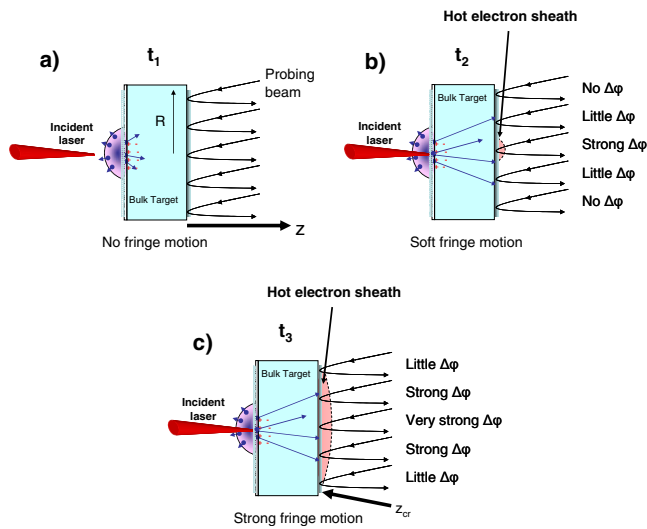


FIG. 3. (Color online) Schematic of the phase measurement. (a) Case of an unperturbed target: the target rear surface acts as a perfect mirror. (b) Case of a weakly perturbed target by the early plasma expansion: the phase shift is significant on the laser axis only, while negligible further away. (c) Case of a strongly expanded target, leading to a pronounced phase shift everywhere, mostly in the central region.

obtain a 1D line that goes through the center of the zone of interest on the rear target surface. Thus we have a radial spatial resolution of the rear target surface along the axis noted R in Fig. 3. The image of the slit is collected by a spherical mirror with focal length $f=1$ m and the collimated light is projected on a grating.

The first diffraction order is sent back to the spherical mirror, which focuses the then spectrally dispersed light onto a 2D CCD. As the chirp of the pulse is linear, we thus have on the 2D CCD one axis that corresponds to the spectral dispersion and hence gives a linear encoding in time. The temporal resolution of the diagnostic is given by the spectral width of our pulse²³ and is in our case

$$\Delta t = \sqrt{\tau_{\text{chirped}} \tau_{\text{compressed}}} = \sqrt{50 \times 10^{-12} * 320 \times 10^{-15}} [\text{s}]$$

$$= 4 \text{ ps.} \quad (1)$$

Since the spectrometer slit is orthogonal to the spectral dispersion plane, on the 2D CCD the other axis corresponds to the 1D radial spatial resolution. The ultimate spatial resolution is given by the optical system characteristics. In our experiment, the outgoing beam is imaged by a $f=250$ mm lens with 75 mm diameter. Therefore, the spatial resolution of the optical system can be calculated by the resolving power that is $\Delta r_{\text{lens}} \approx 1.2\lambda f/D$, where λ is the wavelength, f is the focal length, and D is the aperture of the lens. In our case $\Delta r_{\text{lens}} \approx 5 \mu\text{m}$ and the resolution given by the spectrometer slit width was around $\Delta r_{\text{slit}} \sim 2.3 \mu\text{m}$. We therefore obtain a total spatial resolution of $\Delta r_{\text{tot}} = \sqrt{\Delta r_{\text{lens}}^2 + \Delta r_{\text{slit}}^2} \approx 5.51 \mu\text{m}$.

To obtain spatial phase information at each instant in time, we position the fringes parallel to the dispersion plane, i.e., perpendicular to the spectrometer entrance slit (see Fig. 2). In the case of an unperturbed rear surface, the image after the spectrometer will be simply an image of the target along the axis R with parallel fringes along the spectral, i.e., tem-

poral axis. When the rear target surface starts expanding (see Fig. 3), the overall dephasing of the probe beam changes with time and space, which induces a shift of the fringes (see Fig. 2) that varies along R . A shift of one fringe width corresponds to a phase shift of 2π , i.e., in the case of a probe beam with wavelength of $\lambda_p = 1.057 \mu\text{m}$ the surface motion will be of $1.057 \mu\text{m}$ for normal incidence. For oblique incidence of the probe beam onto the target, this distance is reduced by $\cos \theta$ where θ is the angle between the normal of the target surface and the impinging beam (see Fig. 1).

It is important to choose correctly the magnification of the rear surface image and the number of fringes within the image. A too high magnification does not allow the viewing of the entire zone heated by the electrons and moreover, there is the risk of the two images produced by the Mach-Zehnder of the electron heated zone on the target overlap within the observation field on the CCD thus compromising the information. On the contrary, when the imaged spot is too small, there are only a few fringes over the heated zone and therefore the spatial resolution of the diagnostic is lower.

B. The parameters that modify the probe beam phase

As mentioned in the Introduction, the phase of the probe beam reflecting off the target rear depends on two electron populations (see Fig. 3). First, there is the cloud of laser accelerated hot electrons that break through the target rear surface and expand into vacuum. They are generated at the critical density target front interface, and since they have diverged through the target,^{13,17,18,24} their density becomes lower than the critical density. The probe beam therefore propagates through this electron population before reaching the target rear surface. Second, there is the heated bulk electron population that induces motion of the target bulk onto which the probe beam reflects. The time-dependent modifications induced on the phase of the probe beam propagating in these conditions can be easily derived, as detailed in Appendix A. The TASRI diagnostic measures this phase $\varphi(r, t)$.

C. How the plasma expansion parameters are retrieved from the interferograms

1. General procedure

We first transform, using a Fourier analysis technique detailed in Appendix B, the raw interferograms into phase maps $\Delta\varphi(r, t) = \varphi_{\text{ref}} - \varphi(r, t)$, where φ_{ref} is the reference phase corresponding to the situation where the rear target surface is not in motion and no plasma is generated. An example of such $\Delta\varphi$ phase map is shown in Fig. 4. Due to the configuration of the diagnostic using a Mach-Zehnder (see Fig. 2), the phase map exhibits two mirroring symmetric signals (i.e., the two phase maps carry the same information). The phase $\Delta\varphi$ can be extracted from any of these two phase maps which carry the same information.

Since $\Delta\varphi$ results from an integration process through the expanding hot plasma (see Appendix A), the relation between phase and electron density is not bijective, i.e., different electron density profiles may result in equal phase shifts $\Delta\varphi$. To retrieve the plasma parameters at the start of the

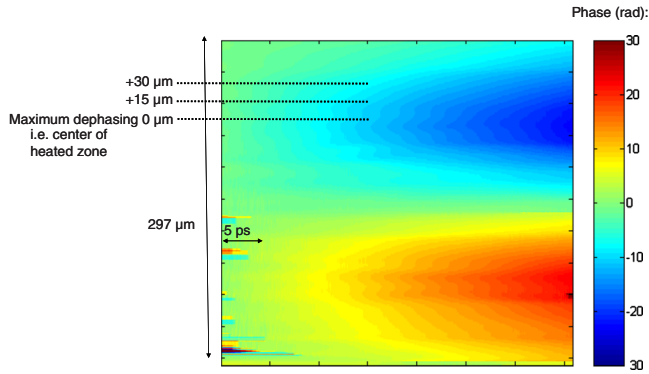


FIG. 4. (Color online) Phase map (in radians) measured from a 25 μm target irradiated with a $5 \times 10^{19} \text{ W/cm}^2$, 320 fs laser pulse. The dotted lines indicate the distance from the center of the heated zone. The top and bottom maps are simply sign reversal of each other.

expansion (n_h^0, T_h^0, T_c^0), we proceed as follows: using as input initial parameters (n_h^0, T_h^0, T_c^0) obtained from analytical estimates (see next section), we run numerical simulations of plasma expansion into vacuum. From this, we obtain plasma density profiles and target bulk motion. We then calculate the phase (dephasing) induced by these density profiles by numerically propagating the probe beam back and forth. We compare the calculated $\Delta\phi$ to the measured ones and modify iteratively the input parameters until we obtain a matching agreement between the two $\Delta\phi$.

2. Analytical estimates of initial parameters

To initiate the numerical simulations of the plasma expansion into vacuum, we need simple estimates of n_h^0 , T_h^0 , and T_c^0 at the beginning of the expansion process. The initial bulk cold electron density n_c^0 is indeed known. For aluminum, we simply consider an ionization degree of 2.4 (as given by the Thomas–Fermi model)²⁵ and atomic density of $6.031 \times 10^{22} \text{ atoms/cm}^3$ which yields to $n_c^0 = 1.4 \times 10^{23} \text{ electrons/cm}^3$ for aluminum at solid density. Regarding the initial hot electron density n_h^0 , we can follow the models of Refs. 26 and 27 where electron propagation from the target front is treated ballistically, taking into account an angular divergence for the electrons within the target. Using $E = 7 \text{ J}$ in the laser focal spot at the target front, a hot electron temperature given by the laser ponderomotive potential²⁸ $T_h^0 = 1.5 \text{ MeV}$ and a sheath radius over which the electrons spread on the target rear surface¹⁰ $r = 100 \mu\text{m}$, we obtain $n_h^0 \sim 5 \times 10^{18} \text{ 1/cm}^3$ at the rear side of a 25 μm thick target. Alternatively, considering that the hot electrons are emitted at the target front side with a density of n_c and with a divergence half-angle of 20° – 40° ,^{13,17,29} we obtain a similar result, i.e., a density of 1 – $10 \times 10^{19} \text{ 1/cm}^3$ at the rear side of the same target. We see that n_h and n_c differ by at least three orders of magnitude, which is consistent with other findings.^{10,31}

Regarding the initial hot electron energy T_h^0 , it can be approximated from the ponderomotive potential or to the value measured in experiments using electron spectrometers, i.e., $T_h^0 \sim 1$ – 2 MeV for a laser intensity of 10^{19} W/cm^2 .¹⁴ Indeed, it has been shown that the high-energy tail of the electron distribution during plasma expansion reflects the

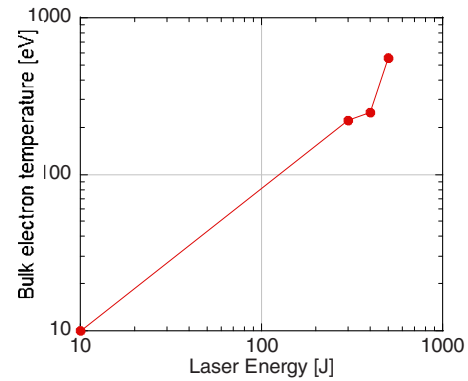


FIG. 5. (Color online) Bulk electron temperature vs laser energy as reported in Refs. 11, 13, 18, and 32 for a target of thickness 30 μm .

initial electron distribution.³⁰ Note that all these estimates are consistent with the values $n_h^0 = 3 \times 10^{19} \text{ 1/cm}^3$ and $T_h^0 = 0.55 \text{ MeV}$ derived independently from proton radiography.³¹

Finally, regarding T_c^0 , previous experimental findings with 100 TW and petawatt-class lasers indicate that the bulk electron temperature (heating of the target) scales as ~ 1 – 2 eV per joule of laser energy (see Fig. 5).^{5,7,11,32} Since in our experiment the laser energy was ~ 5 – 20 J , this scaling would give us $T_c^0 \sim 10 \text{ eV}$. A more accurate estimate follows from numerically solving the coupled electron and ion heat equation, as done in Refs. 33 and 34.

3. Plasma expansion characteristics retrieved from numerical reconstruction of the TASRI phase maps

Using the previously derived initial estimates for n_h^0 , T_h^0 , and T_c^0 , we then perform simulations of plasma expansion into vacuum using the relativistic hybrid 1D code ION-BOOST described in Ref. 35 that models both hot electron expansion and critical density expansion. We used 1D calculations to model a 3D geometry since the expansion is radially symmetric and laminar.³⁶ The symmetry of the expansion is confirmed by the symmetry of the experimental phase map of Fig. 4 with respect to the axis $r=0$. We can therefore restrict our analysis to a 2D cylindrical (r, z) geometry, where r is the radius along the target surface, with $r=0$ being the focal spot center, and z is the plasma expansion axis, perpendicular to r (see Fig. 6). As has been shown in several previous experiments, e.g., in Refs. 31 and 37, the expanding

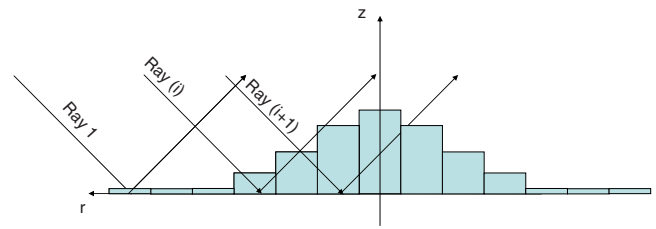


FIG. 6. (Color online) Schematic for the reconstruction of the 2D (r, z, t) density expansion maps from a series of side-by-side 1D (z, t) expansion profiles. Overlaid are shown some rays of the probe beam incident at 45° and propagating in the 2D (r, z, t) density profile. Note that the bins shown in the figure are only a schematic representation, the real calculation being made with a much finer mesh, as shown in Fig. 7.

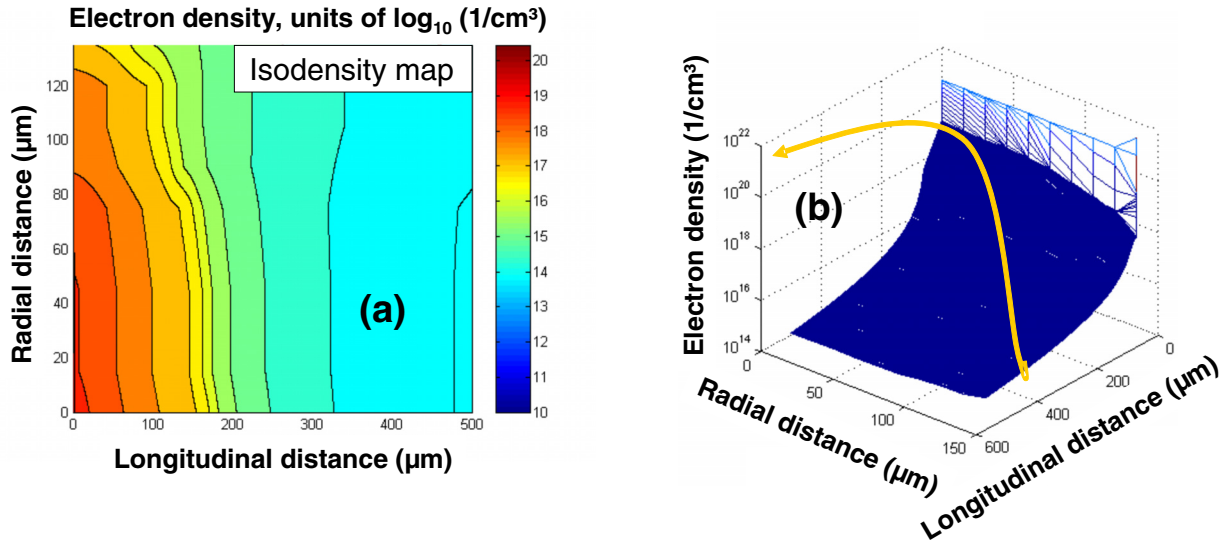


FIG. 7. (Color online) 2D profiles of the expanding plasma obtained by binning electron density profiles retrieved using the 1D model described in Ref. 35. (a) Isodensity contour map corresponding to 20 ps after the start of the expansion and (b) 3D view of the expanding plasma after 8 ps, with the trajectory of one probe beam ray.

plasma, rather than being spherical, is closer to having a Gaussian dependence in the transverse dimension r . The 2D electron density profile $n_e(r, z, t)$ used for calculating the numerical dephasing in the model is therefore built (see Figs. 6 and 7) from a series of 1D (z, t) simulations (as in Ref. 35) that are binned together side-by-side. We stress that the electron temperature and density distributions used in the phase calculations and retrieved from the 1D simulations are not time-integrated but time-resolved. At a later stage of the phase calculations, some time integration over a ~ 4 ps is performed in order to take into account the time resolution of the diagnostic.

Now, in order to determine $n_h^0(r)$, $T_h^0(r)$, and $T_c^0(r)$, we compare, for each instant in time, the calculated phase shifts $\varphi(r, t)$, undergone by the probe beam incident at 45° into the 2D (r, z, t) modeled plasma, to the experimental values. A few probe beam rays used for this calculation are schematically shown in Fig. 6. As the expansion characteristics of various 1D profiles are entangled when calculating $\varphi(r)$, we first perform a series of 1D simulations with various n_h^0 and T_h^0 , which gives us a database of 1D profiles $n_e(z, t)$, therefore, we start with a ray (“ray 1” in Fig. 6) reflecting off the target surface at a point far away from the axis $r=0$, where the hot electron density is low enough so that the phase shift is mostly induced by the bulk electron population (T_c) Doppler shift. Then we calculate the phase for probe beam rays progressively reflecting closer to the center [in Fig. 6, the rays are shown schematically as straight rays but the calculations take fully into account refraction effects, as shown in Fig. 7(b)]. The benefit of performing the calculation progressively from the radial edge of the target toward its center (the irradiation axis) is that we can decompose the phase of each ray, as the phase cumulated on its path before the reflection point (φ_{in}^i for the i th ray) and the phase cumulated after reflection (φ_{out}^i for the i th ray), so that the total phase for this ray is $\varphi^i = \varphi_{\text{in}}^i + \varphi_{\text{out}}^i$. We can see that the phase of the ray (i) going out of the plasma φ_{out}^i can be used to infer the phase of the ray ($i+1$) going in the plasma $\varphi_{\text{in}}^{i+1}$, as can be seen

schematically in Fig. 6. Thus, for the outermost ray experiencing a non-negligible hot electron contribution, only φ_{out}^i will be affected by the hot electrons (for φ_{in}^i only the bulk electrons will contribute). We look up in the database the profiles that allow matching the measured phase $\varphi_{\text{measured}}^i$ to $\varphi_{\text{calculated}}^i$. We then repeat the procedure for rays increasingly closer to the center, using each time φ_{out}^i as an initial guess for $\varphi_{\text{in}}^{i+1}$, and fitting the total phase $\varphi_{\text{calculated}}^i$ to the measured one by modifying the 1D profiles. Thus we can iteratively retrieve the expansion parameters of the successive 1D columns that form the 2D profile. Finally, in order to take into account the resolution of the TASRI (i.e., ~ 4 ps), the simulated phase map is convolved with a Gaussian function having a full width half maximum (FWHM) equal to the time resolution. The convolution will smooth out any abrupt phase changes such as that arising at the start of the expansion.

4. Calculation of the exact dephasing for waves propagating in very steep electron gradients

We should note that our phase calculation assumes (see Appendix A) that the incident probe beam pulse is a perfect sinusoid until it reaches the critical density point n_{cr} . This is valid as long as the density gradient (L) is not very steep, i.e., $L \gg \lambda$, in which case we can use the WKB approximation.^{38–40} As shown in Appendix C, we find that the WKB approximation leads to a phase error between $\pi/2$ and 0.2 (rad) in the range $kL < 0.2$. For larger scale-lengths, the error is small (< 0.2 rad) and decreases rapidly with kL . In our case, $k = \omega/c = 2\pi/\lambda \approx 5.9$ rad/ μm , and therefore the WKB approximation holds as soon as $L > 0.03$ μm . According to the simulations, this threshold is attained rapidly, i.e., within 3–4 ps. This is comparable to our time resolution, which thus validates the WKB approximation.

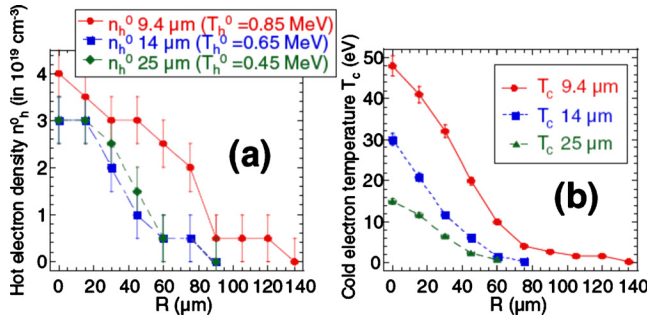


FIG. 8. (Color online) (a) Radial density distribution of the hot electrons initiating the expansion (n_h^0). (b) Bulk electron temperature resulting from target heating. Both are shown for three Al target thicknesses and a laser intensity $\sim 5 \times 10^{19}$ W/cm² with pulse duration $\tau = 320$ fs.

III. RESULTS AND CONCLUSIONS

With the above mentioned diagnostic and taking into account the accuracy of the measurement, we are able to retrieve the hot and warm bulk electron parameters locally at the rear target surface. To illustrate the capability of the diagnostic, we show here results obtained when irradiating aluminum targets with thickness 9.4–25 μm using a laser with intensity of $\sim 5 \times 10^{19}$ W/cm². The wavelength (λ_0) of the laser light was 1.057 μm and the pulse duration was $\tau = 320$ fs, as measured after compression and before focusing. Focusing of the main interaction laser was achieved using a $f/3$ off-axis parabola. Targets positioned at focus were irradiated at normal incidence. Dynamic wave front correction for the laser was applied before every shot.⁴¹ The results are shown in Fig. 8 (extracted from Ref. 10); we see rear target densities ranging up to $\sim 5 \times 10^{19}$ 1/cm³ (with error $\pm 0.5 \times 10^{19}$ 1/cm³) and bulk electron temperatures of up to a few tens of eV (with error bars of $\sim 5\%$) and hot electron temperatures ranging from 0.85 ± 0.2 MeV for the 9.4 μm target to 0.45 ± 0.2 MeV for the thicker target. We observe that T_h^0 is constant for the different probed radii. This is consistent with other measurements.³⁷ Data points have been taken at radial distances of approximately every 6 μm , according to the spatial resolution of the diagnostic. The modeling, used to reproduce the phase shifts, allows having an electron density map, time-integrated within 4 ps, at the target rear surface. It is obvious that the diagnostic can be applied for different kind of targets and laser parameters provided a good reflectivity of the target surface reflecting off the probe beam is ensured. The precision of the TASRI can be used, e.g., for measuring the transverse electron propagation or the electron dilution in mass-limited targets,⁴² becoming hence a powerful tool for determining the dynamics of electrons at the target rear surface.

ACKNOWLEDGMENTS

We acknowledge the expert support of the LULI laser team and the help and useful discussions with J. P. Geindre. This work was supported by Marie Curie Actions, British Council/Egide/Alliance, Grant No. E1127 from Région Ile-de-France, the EU Program No. HPRI CT 1999-0052, projects ELI and SPARX-FEL, and ANR-06-BLAN-0392 from ANR-France.

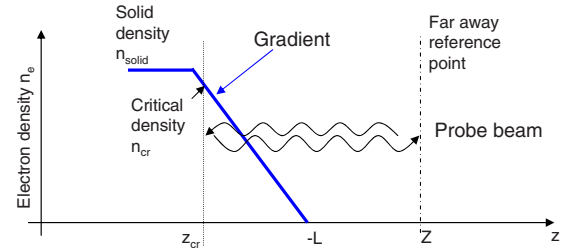


FIG. 9. (Color online) Schematic of an electron density profile, showing how the phase is calculated by integration of the trajectory through the plasma with changing density. The probe beam is coming from the right side.

APPENDIX A: DERIVATION OF THE PHASE SHIFT AND ESTIMATE OF THE IMPORTANCE OF COLLISIONAL EFFECTS

In general, the phase of an electromagnetic wave can be calculated knowing the refractive index of the plasma and by integrating it over the considered trajectory (see Fig. 9). The total phase can be calculated from a far reference point (Z) located in the vacuum up to the probe beam reflection point, i.e., the point where the electron density reaches the critical density (z_{cr}). Note that the symmetric return path has to be added as well. This gives

$$\varphi = 2 \int_{z_{cr}}^Z k dl = 2 \int_{z_{cr}}^Z \frac{\omega}{c} \sqrt{\varepsilon} dl, \quad (\text{A1})$$

where ω is the laser frequency, c is the velocity of light, ε is the dielectric constant, Z is the far reference point in vacuum, z_{cr} is the point in the plasma where the light wave is reflected back, i.e., at the critical density n_{cr} defined as

$$n_{cr} = \frac{m_e \varepsilon_0}{e^2} \omega^2, \quad (\text{A2})$$

with e being the electron charge. In the case of an oblique incident beam with angle θ with respect to the normal target direction, and for the s polarization, the critical density is given by

$$n_{cr_oblique} = n_{cr} [1 - \sin^2(\theta)]. \quad (\text{A3})$$

While the dielectric constant is in general defined as

$$\varepsilon = 1 - \frac{\omega_{pe}^2}{\omega^2 \left(1 - i \frac{\nu}{\omega} \right)} = 1 - \frac{n_e}{n_{cr} \left(1 - i \frac{\nu}{\omega} \right)}, \quad (\text{A4})$$

where $\nu = \nu_{ei} + \nu_{ee}$ denotes the total (electron-ion and electron-electron) collision frequency, n_e the electronic density, i the imaginary unit, and ω_{pe} the electron plasma frequency. In the collisionless case $\nu \ll 1$ and therefore Eq. (A4) simplifies to

$$\varepsilon = 1 - \frac{n_e}{n_{cr}}. \quad (\text{A5})$$

Let us consider in which case this simplification is valid.

In similar fashion to Ref. 18, the total collision frequency involved in Eq. (A4) is calculated by summing the electron-ion and electron-electron collision frequencies relevant for a given phase. The former is given by the Lee and

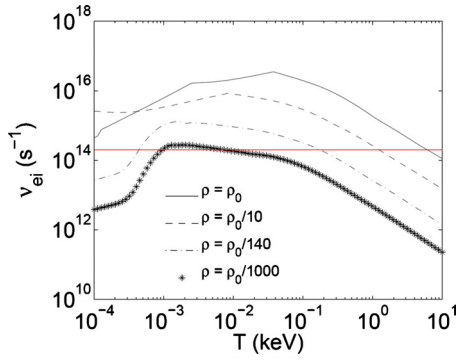


FIG. 10. (Color online) Total collision frequency vs temperature for various densities of the Al target (see text for a description of the collision model). The density ρ_0 corresponds to the Al solid density, i.e., to an electron density of $\sim 1.4 \times 10^{23} \text{ cm}^{-3}$. Above the red line, collisional effects cannot be neglected in the dephasing calculation.

More model⁴³ in the whole temperature range, while the latter is computed from the formula derived in Ref. 44 in the plasma phase and the approximation $\nu_{ee} = k_B T_e^2 \hbar \epsilon_F$ (where k_B denotes the Boltzmann constant, T_e the electron temperature, \hbar the Planck constant, and ϵ_F the Fermi energy) in the solid/liquid phase.⁴⁵ The resulting collision frequency is plotted in Fig. 10 as a function of the bulk temperature for varying values of the Al mass density ρ . The reference density ρ_0 is taken to be the density of solid aluminum. In the cold limit, assuming an ionization degree $Z^* = 2.4$ (as given by the Thomas–Fermi model),²⁵ this corresponds to an electron density of $\sim 1.4 \times 10^{23} \text{ 1/cm}^3$. Given the weak ($< 20\%$) variation of Z^* in the range $0 < T_c < \sim 10 \text{ eV}$,²⁵ the $\rho_0/140$ curve approximately corresponds to $n_e \sim n_{cr}$, that is, the maximum density reached by the $1.053 \text{ } \mu\text{m}$ laser pulse. The condition for negligible collisions (i.e., assuming a contribution smaller than 10%, when $\nu/\omega < 0.1$) which leads to Eq. (A5) instead of Eq. (A4), is equivalent to $\nu < 2 \times 10^{14} \text{ s}^{-1}$. This threshold value is indicated with the red solid horizontal line in Fig. 10 and is verified for a bulk temperature range of $T_c < \sim 0.5 \text{ eV}$ and $T_c > \sim 20 \text{ eV}$.

We now quantify the collisional effects on the total dephasing of a probe beam traveling through a simulated density profile. Figure 11(a) compares the dephasing computed numerically for two cases, both using $T_h = 0.45 \text{ MeV}$ and $n_h = 10^{20} \text{ 1/cm}^3$, but the first one with and the second without collisions. This means that for the first case the calculation has been computed using Eq. (A4), for the second one using Eq. (A5). In both cases, T_c is fixed at 2 eV , i.e., the value maximizing ν_{ei} (see Fig. 10). We see that the collision-

less model yields to a stronger dephasing compared to the case with collisions due to the absorption. The difference between both cases, after $\sim 45 \text{ ps}$, is 13 rad compared to 10 rad , i.e., $\sim 3 \text{ rad}$ ($\sim 30\%$).

The same comparison is made in Fig. 11(b) for $T_c = 10 \text{ eV}$. Both curves now almost coincide, the difference in dephasing being $< 1\%$ after 45 ps . Note that the absolute value of the dephasing is somewhat stronger than in Fig. 11(a). Hence we can assess that when using bulk electron populations $> 10 \text{ eV}$ ion-electron collisions can be neglected in the phase calculations.

APPENDIX B: FOURIER ANALYSIS OF INTERFEROGRAMS TO RETRIEVE PHASE MAPS

To measure the modifications $\Delta\varphi$ induced on the probe beam phase by the reflection on the laser-irradiated foil, we will evaluate the difference between the actual probe beam phase and a reference phase that is obtained by measuring the phase relative to an unperturbed part of the surface. The latter is obtained from a lineout (in the interferogram shown in Fig. 2 it is a vertical lineout) of the unperturbed part of the interferogram, which is a signal of the type

$$a_{\text{ref}}(r) = \cos(k_0 r), \quad (\text{B1})$$

where r is the radial distance from the center of the target and k_0 is the wave number at fundamental frequency of the interference pattern. Perturbations of the target rear surface will induce a shift of the fringes. If we perform a lineout of the signal at a given time, the phase of the cosinusoid is then modified to be

$$a_{\text{data}}(r, t) = \cos[k_0 r + \Delta\varphi(r, t)], \quad (\text{B2})$$

where the phase shift $\Delta\varphi$ is added to the regular phase pattern $k_0 r$. It is therefore easy to identify it in the phase domain as a modification of the phase around the carrier component at $k = k_0$. This is performed using a Fourier-transform (FT) to obtain

$$\text{FT}_{\text{reference}}[\cos(k_0 r)] = \frac{\delta(k - k_0) + \delta(k + k_0)}{2} \quad (\text{B3})$$

and

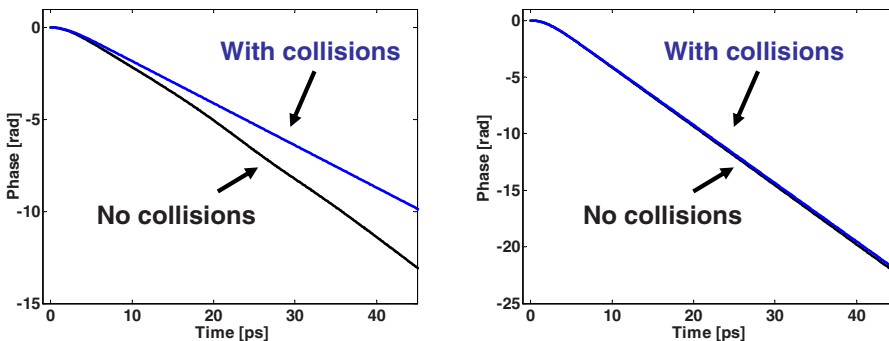


FIG. 11. (Color online) (a) Influence of collisions on the dephasing computed with $T_h = 0.45 \text{ MeV}$, $n_h = 10^{20} \text{ cm}^{-3}$, and $T_c = 2 \text{ eV}$. (b) Same as (a) but with $T_c = 10 \text{ eV}$.

$$\begin{aligned}
& \text{FT}_{\text{signal}}\{\cos[k_0 r + \Delta\varphi(r, t)]\} \\
&= \text{FT}\left(\frac{e^{ik_0 r} e^{i\Delta\varphi(r, t)} + e^{-ik_0 r} e^{-i\Delta\varphi(r, t)}}{2}\right) \\
&= \frac{\delta(k - k_0) \otimes \text{FFT}(e^{i\Delta\varphi(r, t)}) + \delta(k + k_0) \otimes \text{FFT}(e^{-i\Delta\varphi(r, t)})}{2},
\end{aligned} \quad (\text{B4})$$

where \otimes means the convolution product. We obtain in both cases a spectrum with two Dirac-functions, one located around a central carrier frequency k_0 and the other around $-k_0$. The information contained in each Dirac-function is the same. To get the information we therefore only need to select one of those two Dirac-functions and perform an inverse Fourier-transform. Considering, e.g., only the negative carrier, we obtain two exponential functions for the reference and the signal

$$\text{FT}_{\text{signal}}^{-1}[\delta(k - k_0) \otimes e^{i\Delta\varphi(r, t)}] = e^{i[k_0 r + \Delta\varphi(r, t)]}, \quad (\text{B5})$$

$$\text{FT}_{\text{reference}}^{-1}[\delta(k - k_0)] = e^{ik_0 r}. \quad (\text{B6})$$

If we divide these exponential functions, we can retrieve $\Delta\varphi$,

$$\text{Im}\left[\ln\left(\frac{e^{i(k_0 r + \varphi)}}{e^{ik_0 r}}\right)\right] = \Delta\varphi(r, t) \quad (\text{B7})$$

APPENDIX C: VALIDITY OF THE WKB APPROXIMATION IN STEEP GRADIENTS

The WKB approximation is not always verified, especially at the beginning of the expansion (when $L = c_s t$ is $< 1 \mu\text{m}$). Hence, it is important to estimate the error due to this approximation. We here consider the case of a linearly increasing electron density gradient onto which the wave is incident (see Fig. 9). Since the wave is traveling partially in vacuum and partially in a dense plasma, we need to connect both waves in a continuous manner.

The basic scheme of the gradient is [considering $\varepsilon = 1 - n_e/n_{\text{cr}}$, see Eq. (A5)]

$$\begin{aligned}
\varepsilon = 1 \quad n_e = 0 & \quad \text{For } z < -L \\
\varepsilon = -\frac{z}{L} \quad n_e \text{ increases linearly to } n_{\text{cr}} & \quad \text{For } -L \leq z \leq 0. \\
\varepsilon = 0 \quad n_e = n_{\text{cr}} & \quad \text{For } z > 0
\end{aligned} \quad (\text{C1})$$

In the plasma ($z > -L$) the solution of the electric field is an Airy function with^{46,47}

$$E \propto \text{Re}[A_i(\eta)e^{-i\omega t}], \quad \text{with} \quad (\text{C2})$$

$$\eta = \left(\frac{\omega^2}{c^2 L}\right)^{1/3} z = \frac{(kL)^{2/3}}{L} z, \quad (\text{C3})$$

for normal incidence. We will concentrate on the case of normal incidence and without collisions. To consider oblique incidence the variable η should be replaced by

$$\eta = (kL)^{2/3} \left(\frac{z}{L} - \sin^2 \theta\right). \quad (\text{C4})$$

In the case of oblique incidence and non-negligible collisions, η can be written as⁴⁸

$$\eta = (kL)^{2/3} \left(1 - i\frac{\nu}{\omega}\right)^{-1/3} \left[\frac{z}{L} - \sin^2(\theta) + i\frac{\nu}{\omega} \cos^2(\theta)\right]. \quad (\text{C5})$$

Considering $|kL| \gg 1$, i.e., when the gradient is not very steep or the wave number very big, the WKB approximation leads to the following asymptotic behavior:

$$A_i(\eta) \propto \cos\left(\frac{2}{3}\xi^{3/2} - \frac{\pi}{4}\right), \quad (\text{C6})$$

with

$$\xi = -\eta = -\left(\frac{\omega^2}{c^2 L}\right)^{1/3} z = \left(\frac{\omega^2}{c^2 L}\right)^{1/3} |z|. \quad (\text{C7})$$

In vacuum ($z < -L$) we have an electromagnetic wave generated by the superposition of the incident and reflected waves, with an electric field of the form,

$$E \propto \text{Re}[(e^{ikz} + e^{-i(kz+\varphi)})e^{-i\omega t}],$$

or taking only its real part

$$E \propto \text{Re}\left[\cos\left(kz - \frac{\varphi}{2}\right)e^{-i\omega t}\right] \propto C \cos\left(kz - \frac{\varphi}{2}\right), \quad (\text{C8})$$

with its derivate

$$\frac{\partial E}{\partial z} \propto -kC \sin\left(kz - \frac{\varphi}{2}\right).$$

The electric field E and its derivative are continuous in $z = -L$, i.e., we need to connect the plasma wave function $A_i(\eta)$ for ($z > -L$) using Eq. (C7) which yields to

$$A_i(\eta)|_{z=-L} = C \cos\left(-kL - \frac{\varphi}{2}\right), \quad (\text{C9})$$

and consequently also the derivative, which becomes

$$\left.\frac{dA_i(\eta)}{dz}\right|_{z=-L} = -Ck \sin\left(-kL - \frac{\varphi}{2}\right). \quad (\text{C10})$$

The derivative of the Airy function in Eq. (C10) is done for the variable z . The derivative with respect to the variable η , considering Eq. (C5) becomes

$$\left(\frac{1}{kL}\right)^{1/3} \left.\frac{dA_i(\eta)}{d\eta}\right|_{\eta=\eta_L} = -C \sin\left(-kL - \frac{\varphi}{2}\right). \quad (\text{C11})$$

Dividing Eq. (C11) by Eq. (C9) one obtains

$$kL + \frac{\varphi}{2} = \arctan\left[\frac{\left.\frac{dA_i(\eta)}{d\eta}\right|_{\eta=\eta_L}}{(kL)^{1/3} \cdot A_i(\eta_L)}\right], \quad (\text{C12})$$

with the intersection point $z = -L$ becoming

$$\eta_L = \left(\frac{\omega^2}{c^2 L}\right)^{1/3} (-L) = -(kL)^{2/3}. \quad (\text{C13})$$

There follows the expression of the dephasing

$$\varphi = 2 \left\{ \arctan\left[\frac{\left.\frac{dA_i(\eta)}{d\eta}\right|_{\eta=\eta_L}}{(kL)^{1/3} \cdot A_i(\eta_L)}\right] - kL \right\}. \quad (\text{C14})$$

Plots of φ as calculated from Eq. (C14) are shown Fig. 12.

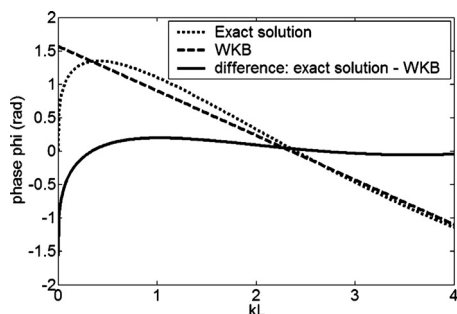


FIG. 12. Plots of the phase of the exact solution (dotted line) given by Eq. (C14), WKB approximation (dashed line) and the difference between both (solid line) as a function of kL (in this case $\lambda=1.058 \mu\text{m}$ and $k=5.9 \text{ rad}/\mu\text{m}$).

For small gradients, the error between the exact (Airy) solution and the WKB solution is $\pi/2$. As expected, the error decreases with increasing kL . A closer look reveals that the exact solution oscillates around the approximated WKB curve converging more and more to the approximation (see in Fig. 12 the dotted line above the dashed line for $kL < 2.5$ and below for $kL > 2.5$). This has also been observed experimentally. We have verified the results of Fig. 12 by solving numerically the wave equation

$$\frac{\partial^2 E_x}{\partial z^2} + \frac{\omega^2}{c^2} \varepsilon(\omega, z) E_x = 0, \quad (\text{C15})$$

using a Runge–Kutta solver. The reference phase is calculated using $n_e \ll 1$, i.e., $\varepsilon(\omega, z)=1$ at a location far from the injection surface. This reference phase is then subtracted from the phase calculated at the same location but using the spatially dependent dielectric constant $\varepsilon(\omega, z)$. The results thus obtained closely agree with the analytical results of Fig. 12 for all kL values.⁴⁷ In addition, we point out that the use of a linearly changing density instead of an exponential is a valid approximation since in the vicinity of the reflection point, the gradient can be considered to be linear within the oscillation of the wave.

- ¹F. Floux, D. Cognard, L.-G. Denoed, G. Piar, D. Parisot, J. M. Bobin, F. Delobbeau, and C. Fauquignon, *Phys. Rev. A* **1**, 821 (1970).
- ²M. Tabak, J. Hammer, M. E. Glinsky, W. L. Kruer, S. C. Wilks, J. Woodworth, E. M. Campbell, M. D. Perry, and R. J. Mason, *Phys. Plasmas* **1**, 1626 (1994).
- ³M. Roth, T. E. Cowan, M. H. Key, S. P. Hatchett, C. Brown, W. Fountain, J. Johnson, D. M. Pennington, R. A. Snavely, S. C. Wilks, K. Yasuike, H. Ruhl, F. Pegoraro, S. V. Bulanov, E. M. Campbell, M. D. Perry, and H. Powell, *Phys. Rev. Lett.* **86**, 436 (2001).
- ⁴P. Mora, *Phys. Rev. Lett.* **90**, 185002 (2003).
- ⁵M. Borghesi, J. Fuchs, S. V. Bulanov, A. J. MacKinnon, P. K. Patel, and M. Roth, *Fusion Sci. Technol.* **49**, 412 (2006).
- ⁶S. N. Chen, G. Gregori, P. K. Patel, H.-K. Chung, R. G. Evans, R. R. Freeman, E. Garcia Saiz, S. H. Glenzer, S. B. Hansen, F. Y. Khattak, J. A. King, A. J. MacKinnon, M. M. Notley, J. R. Pasley, D. Riley, R. B. Stephens, R. L. Weber, S. C. Wilks, and F. N. Beg, *Phys. Plasmas* **14**, 102701 (2007).
- ⁷P. K. Patel, A. J. MacKinnon, M. H. Key, T. E. Cowan, M. E. Ford, M. Allen, D. F. Price, H. Ruhl, P. T. Springer, and R. Stephens, *Phys. Rev. Lett.* **91**, 125004 (2003).
- ⁸A. Mančić, A. Lévy, M. Harmand, M. Nakatsutsumi, P. Antici, P. Audebert, P. Combis, S. Fourmaux, S. Mazevet, O. Peyrusse, V. Recoules, P. Renaudin, J. Robiche, F. Dorchies, and J. Fuchs, *Phys. Rev. Lett.* **104**, 035002 (2010); P. Antici, J. Fuchs, S. Atzeni, A. Benuzzi, E. Brambrink, M. Esposito, M. Koenig, A. Ravasio, J. Schreiber, A. Schiavi and P. Audebert, *ECA* **29C**, 0-3.003 (2005).

- ⁹P. Antici, J. Fuchs, S. Atzeni, A. Benuzzi, E. Brambrink, M. Esposito, M. Koenig, A. Ravasio, J. Schreiber, A. Schiavi, and P. Audebert, *J. Phys. IV* **133**, 1077 (2006).
- ¹⁰P. Antici, J. Fuchs, M. Borghesi, L. Gremillet, T. Grismayer, Y. Sentoku, E. d'Humières, C. A. Cecchetti, A. Mancic, A. C. Pipahl, O. Willi, P. Mora, and P. Audebert, *Phys. Rev. Lett.* **101**, 105004 (2008).
- ¹¹J. A. Koch, M. H. Key, R. R. Freeman, S. P. Hatchett, R. W. Lee, D. Pennington, R. B. Stephens, and M. Tabak, *Phys. Rev. E* **65**, 016410 (2001).
- ¹²G. Malka and J. L. Miquel, *Phys. Rev. Lett.* **77**, 75 (1996).
- ¹³M. H. Key, M. D. Cable, T. E. Cowan, K. G. Estabrook, B. A. Hammel, S. P. Hatchett, E. A. Henry, D. E. Hinkel, J. D. Kilkenny, J. A. Koch, W. L. Kruer, A. B. Langdon, B. F. Lasinski, R. W. Lee, B. J. MacGowan, A. MacKinnon, J. D. Moody, M. J. Moran, A. A. Offenberger, D. M. Pennington, M. D. Perry, T. J. Phillips, T. C. Sangster, M. S. Singh, M. A. Stoyer, M. Tabak, G. L. Tietbohl, M. Tsukamoto, K. Wharton, and S. C. Wilks, *Phys. Plasmas* **5**, 1966 (1998).
- ¹⁴M. Allen, Y. Sentoku, P. Audebert, A. Blazevic, T. Cowan, J. Fuchs, J. C. Gauthier, M. Geissel, M. Hegelich, S. Karsch, E. Morse, P. K. Patel, and M. Roth, *Phys. Plasmas* **10**, 3283 (2003).
- ¹⁵H. Popescu, S. D. Baton, F. Amiranoff, C. Rousseaux, M. Rabec Le Gloahéc, J. J. Santos, L. Gremillet, M. Koenig, E. Martinolli, T. Hall, J. C. Adam, A. Heron, and D. Batani, *Phys. Plasmas* **12**, 063106 (2005).
- ¹⁶H. Habara, K. Ohta, K. A. Tanaka, G. Ravindra Kumar, M. Krishnamurthy, S. Kahaly, S. Mondal, M. Kumar Bhuyan, R. Rajeev, and J. Zheng, *Phys. Rev. Lett.* **104**, 055001 (2010).
- ¹⁷R. B. Stephens, R. A. Snavely, Y. Aglitskiy, F. Amiranoff, C. Andersen, D. Batani, S. D. Baton, T. Cowan, R. R. Freeman, T. Hall, S. P. Hatchett, J. M. Hill, M. H. Key, J. A. King, J. A. Koch, M. Koenig, A. J. MacKinnon, K. L. Lancaster, E. Martinolli, P. Norreys, E. Perelli-Cippo, M. Rabec Le Gloahéc, C. Rousseaux, J. J. Santos, and F. Scianitti, *Phys. Rev. E* **69**, 066414 (2004).
- ¹⁸E. Martinolli, M. Koenig, S. D. Baton, J. J. Santos, F. Amiranoff, D. Batani, E. Perelli-Cippo, F. Scianitti, L. Gremillet, R. Mèlizzi, A. Decoster, C. Rousseaux, T. A. Hall, M. H. Key, R. Snavely, A. J. MacKinnon, R. R. Freeman, J. A. King, R. Stephens, D. Neely, and R. J. Clarke, *Phys. Rev. E* **73**, 046402 (2006).
- ¹⁹F. Pisani, A. Bernardinello, D. Batani, A. Antonicci, E. Martinolli, M. Koenig, L. Gremillet, F. Amiranoff, S. Baton, J. Davies, T. Hall, D. Scott, P. Norreys, A. Djaoui, C. Rousseaux, P. Fewes, H. Bandulet, and H. Pepin, *Phys. Rev. E* **62**, R5927 (2000).
- ²⁰K. Yasuike, M. H. Key, S. P. Hatchett, R. A. Snavely, and K. B. Wharton, *Rev. Sci. Instrum.* **72**, 1236 (2001).
- ²¹M. I. K. Santala, M. Zepf, I. Watts, F. N. Beg, E. Clark, M. Tatarakis, K. Krushelnick, A. E. Dangor, T. McCanny, I. Spencer, R. P. Singhal, K. W. D. Ledingham, S. C. Wilks, A. C. Machacek, J. S. Wark, R. Allott, R. J. Clarke, and P. A. Norreys, *Phys. Rev. Lett.* **84**, 1459 (2000).
- ²²J. J. Santos, F. Amiranoff, S. D. Baton, L. Gremillet, M. Koenig, E. Martinolli, M. Rabec Le Gloahéc, C. Rousseaux, D. Batani, A. Bernardinello, G. Greison, and T. Hall, *Phys. Rev. Lett.* **89**, 025001 (2002).
- ²³J. P. Geindre, P. Audebert, S. Rebibo, and J.-C. Gauthier, *Opt. Lett.* **26**, 1612 (2001).
- ²⁴G. Malka, Ph. Nicolaï, E. Brambrink, J. J. Santos, M. M. Aléonard, K. Amthor, P. Audebert, J. Breil, G. Claverie, M. Gerbaux, F. Gobet, F. Hannachi, V. Méot, P. Morel, J. N. Scheurer, M. Tarisien, and V. Tikhonchuk, *Phys. Rev. E* **77**, 026408 (2008).
- ²⁵F. Röhrlich and B. C. Carlson, *Phys. Rev.* **93**, 38 (1954); S. M. Seltzer, "Transmission of electrons through foils," National Bureau of Standards Rapport Technique Report No. COM-74-11792, 1974; J. F. Ziegler, *J. Appl. Phys.* **85**, 1249 (1999); T. A. Mehlhorn, *ibid.* **52**, 6522 (1981).
- ²⁶M. Kaluza, J. Schreiber, M. I. K. Santala, G. D. Tsakiris, K. Eidmann, J. Meyer-ter-Vehn, and K. J. Witte, *Phys. Rev. Lett.* **93**, 045003 (2004).
- ²⁷J. Fuchs, P. Antici, E. D'Humières, E. Lefebvre, M. Borghesi, E. Brambrink, C. A. Cecchetti, M. Kaluza, V. Malka, M. Manclossi, S. Meyroneinc, P. Mora, J. Schreiber, T. Toncian, H. Pépin, and P. Audebert, *Nat. Phys.* **2**, 48 (2006); J. Fuchs, Y. Sentoku, E. d'Humières, T. E. Cowan, J. Cobble, P. Audebert, A. Kemp, A. Nikroo, P. Antici, E. Brambrink, A. Blazevic, E. M. Campbell, J. C. Fernández, J.-C. Gauthier, M. Geissel, M. Hegelich, S. Karsch, H. Popescu, N. Renard-LeGalloudec, M. Roth, J. Schreiber, R. Stephens, and H. Pépin, *Phys. Plasmas* **14**, 053105 (2007).
- ²⁸S. C. Wilks, W. L. Kruer, M. Tabak, and A. B. Langdon, *Phys. Rev. Lett.* **69**, 1383 (1992).
- ²⁹J. C. Adam, A. Héron, and G. Laval, *Phys. Rev. Lett.* **97**, 205006 (2006).

- ³⁰T. Grismayer, P. Mora, J. C. Adam, and A. Héron, *Phys. Rev. E* **77**, 066407 (2008).
- ³¹L. Romagnani, J. Fuchs, M. Borghesi, P. Antici, P. Audebert, F. Ceccherini, T. Cowan, T. Grismayer, S. Kar, A. Macchi, P. Mora, G. Pretzler, A. Schiavi, T. Toncian, and O. Willi, *Phys. Rev. Lett.* **95**, 195001 (2005).
- ³²R. G. Evans, E. L. Clark, R. T. Eagleton, A. M. Dunne, R. D. Edwards, W. J. Garbett, T. J. Goldsack, S. James, C. C. Smith, B. R. Thomas, R. Clarke, D. J. Neely, and S. J. Rose, *Appl. Phys. Lett.* **86**, 191505 (2005).
- ³³A. J. Kemp, J. Fuchs, Y. Sentoku, V. Sotnikov, M. Bakeman, P. Antici, and T. E. Cowan, *Phys. Rev. E* **75**, 056401 (2007).
- ³⁴H. Chen and S. C. Wilks, *Laser Part. Beams* **23**, 411 (2005).
- ³⁵P. Mora, *Phys. Rev. E* **72**, 056401 (2005).
- ³⁶T. E. Cowan, J. Fuchs, H. Ruhl, A. Kemp, P. Audebert, M. Roth, R. Stephens, I. Barton, A. Blazevic, E. Brambrink, J. Cobble, J. Fernandez, J.-C. Gauthier, M. Geissel, M. Hegelich, J. Kaae, S. Karsch, G. P. Le Sage, S. Letzring, M. Manclossi, S. Meyroneinc, A. Newkirk, H. Pépin, and N. Renard-LeGalloudec, *Phys. Rev. Lett.* **92**, 204801 (2004).
- ³⁷D. C. Carroll, P. McKenna, O. Lundh, F. Lindau, C.-G. Wahlström, S. Bandyopadhyay, D. Pepler, D. Neely, S. Kar, P. T. Simpson, K. Markey, M. Zepf, C. Bellei, R. G. Evans, R. Redaelli, D. Batani, M. H. Xu, and Y. T. Li, *Phys. Rev. E* **76**, 065401 (2007).
- ³⁸L. Brillouin, *Comptes Rendus de l'Academie des Sciences* **183**, 24 (1926); J. L. Dunham, *Phys. Rev.* **41**, 713 (1932).
- ³⁹H. A. Kramers, *Z. Phys.* **39**, 828 (1926).
- ⁴⁰G. Wentzel, *Z. Phys.* **38**, 518 (1926).
- ⁴¹B. Wattellier, J. Fuchs, J. P. Zou, K. Abdeli, H. Pépin, and C. Haefner, *Opt. Lett.* **29**, 2494 (2004).
- ⁴²S. Buffechoux, J. Psikal, M. Nakatsutsumi, L. Romagnani, A. Andreev, K. Zeil, M. Amin, P. Antici, T. Burris-Mog, A. Compant-La-Fontaine, E. d'Humieres, S. Fourmaux, S. Gaillard, F. Gobet, F. Hannachi, S. Kraft, A. Mancic, C. Plaisir, G. Sarri, M. Tarisien, T. Toncian, U. Schramm, M. Tampo, P. Audebert, O. Willi, T. E. Cowan, H. Pépin, V. Tikhonchuk, M. Borghesi, and J. Fuchs, *Phys. Rev. Lett.* **105**, 015005 (2010).
- ⁴³Y. T. Lee and R. M. More, *Phys. Fluids* **27**, 1273 (1984).
- ⁴⁴A. Decoster, *Modeling of Collisions* (Elsevier-Gauthier-Villars, Paris, 1998).
- ⁴⁵A. P. Kanavin, I. V. Smetanin, V. A. Isakov, Y. V. Afanasiev, B. N. Chichkov, B. Wellegehausen, S. Nolte, C. Momma, and A. Tunnermann, *Phys. Rev. B* **57**, 14698 (1998).
- ⁴⁶P. Mora, *Introduction aux plasmas créés par laser*, 2006.
- ⁴⁷P. Antici, Ph.D. thesis, edited by Ecole Polytechnique, 2007.
- ⁴⁸C. Labaune, "Interaction laser-plasma dans le contexte de la fusion par confinement inertiel," *Proceedings of the Ecole des Houches*, 2005.